

Robust High Dynamic Range Imaging by Rank Minimization

Tae-Hyun Oh *Student Member, IEEE*, Joon-Young Lee *Student Member, IEEE*,
Yu-Wing Tai *Senior Member, IEEE*, and In So Kweon *Member, IEEE*

Abstract—This paper introduces a new high dynamic range (HDR) imaging algorithm which utilizes rank minimization. Assuming a camera responses linearly to scene radiance, the input low dynamic range (LDR) images captured with different exposure time exhibit a linear dependency and form a rank-1 matrix when stacking intensity of each corresponding pixel together. In practice, misalignments caused by camera motion, presences of moving objects, saturations and image noise break the rank-1 structure of the LDR images. To address these problems, we present a rank minimization algorithm which simultaneously aligns LDR images and detects outliers for robust HDR generation. We evaluate the performances of our algorithm systematically using synthetic examples and qualitatively compare our results with results from the state-of-the-art HDR algorithms using challenging real world examples.

Index Terms—High Dynamic Range Image, Rank minimization, RPCA, Matrix Completion, Multi-exposure fusion, Alignment.

1 INTRODUCTION

RADIANCE of a natural scene typically has a wider dynamic range than the dynamic range of cameras that can be recorded. One solution to obtain a full radiance map is to capture multiple low dynamic range (LDR) images at different exposures and merge them to reconstruct a high dynamic range (HDR) image. Over the past decades, there have been a lot of works targeting high dynamic range imaging. Representative works include [1], [2], [3], [4], [5], [6], [7], [8], [9].

Since the multiple LDR images were captured sequentially with different exposure time, there is potential for camera motion across images which leads to misalignment artifacts. Moreover, when there are moving objects in a scene, ghosting artifacts are unavoidable unless special treatments were taken to detect the moving objects. The different noise levels across the LDR images and saturated regions also place additional challenges in the HDR imaging problem.

In this paper, we present an Intensity Observation Model (IOM) which describes the image acquisition process of cameras from sensor irradiance to image intensity. By assuming a linear camera response function (CRF), LDR images are linearly dependent in the ideal case for HDR generation. The linear dependency of LDR images forms a rank-1 matrix when stacking intensity of each corresponding pixel together as illustrated in Fig. 1. We formulate the HDR generation problem into a rank minimization problem where misalignment errors, moving objects, noise and other nonlinear artifacts are considered as sparse outliers. Our

goal is to estimate a rank-1 observation matrix such that the LDR observations are clean and geometrically well aligned. In this work, we assume the alignment can be achieved by using the homography registration. The major benefits of our approach are that it unifies the alignment and outlier rejection processes in HDR and it is robust to sparse errors. When saturated regions or moving objects are largely overlapped across images, the rank minimization algorithm may consider the outliers as inliers. To this end, we have also proposed a low rank matrix completion algorithm which considers saturated regions and moving objects as missing entries and use matrix completion (MC) to recover a low rank matrix. Our algorithm is flexible to handle user inputs to include or remove certain moving objects in the final HDR images.

We test the performance of our algorithm systematically using synthetic examples and qualitatively compare our results with results from the state-of-the-art HDR algorithms using challenging real world examples. We evaluate the performance of our algorithm for alignment, HDR background (latent) image decomposition and HDR composition. Also, we analyze how the radiometric calibration affects the performance of our method. In addition, we have generated synthetic LDR images from a ground truth HDR image, and show quantitative comparisons with a recent commercial program, Photoshop CS6.

Shorter versions of this work appeared in [10], [11]. This paper extends [10], [11] with deeper analyses to our algorithm focusing on the HDR generation problem, further technical details of our implementation, and additional experimentations and evaluations. In addition, a new algorithm on low rank matrix completion is introduced which facilitates user control to reconstruct pseudo LDR images of moving objects under different exposures. This allows us to reconstruct a well aligned ghost-free HDR image with inclusion of selected moving objects.

• T.-H. Oh¹, J.-Y. Lee², Y.-W. Tai³ and I.S. Kweon⁴ are with the Department of Electrical Engineering, Korea Advanced Institute of Science and Technology (KAIST), Daejeon, Republic of Korea.

Project page: <http://thoh.kaist.ac.kr/Research/RHDR/RHDR.htm>

¹(Contact: thoh.kaist.ac.kr@gmail.com, <http://thoh.kaist.ac.kr>)

²(Contact: jylee@rcv.kaist.ac.kr)

³(Contact: yuwwing@kaist.ac.kr)

⁴(Corresponding Author, Contact: iskweon77@kaist.ac.kr)

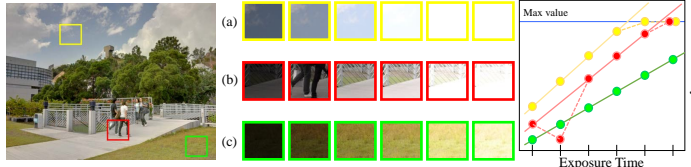


Fig. 1: Illustration of the observed intensity values for (a) saturation region, (b) moving object, and (c) consistent cases. Solid lines denote the ideal relationship between intensity and exposure time, and dots and dotted lines denote the observed intensity samples.

2 RELATED WORKS

There are broad literatures dedicated to the HDR imaging problem. Early works by Mann and Picard [1] andDebevec and Malik [2] estimate camera response function and compose a radiance map from multi-exposure images for a static scene with a static camera. Simultaneously, they have also introduced the tone mapping to compress the dynamic range of the estimated HDR image to LDR using nonlinear tone curve for HDR display purpose. Since our goal is HDR generation, we focus our review to algorithms related to the HDR generation and omit the review in the tone mapping and high dynamic range compression literature. We refer readers to [12] for a complete review of the HDR imaging problem.

Due to the static camera limitation, Mitsunaga and Nayar [13] consider camera global motion to register images with different exposure before creating a HDR image. Ward [8] presents a translation based alignment algorithm to account for camera motion among multi-exposure images. This work is later extended to handle rotational motion by Jacobs *et al.* [9]. Tomaszewska and Mantiuk [14] use key-points to find homography transformations between LDR images for registration. In practice, camera motion is complicated where a global motion model might not perform well in registration especially when camera center is moving. Kang *et al.* [15] estimate pixel-wise displacements between different LDR video frames for HDR video generation. Since differently exposed images do not follow the brightness consistency assumption [16] in motion estimation, Kang *et al.* transform intensities of LDR images to luminance domain using exposure time information for robust motion estimation. Zimmer *et al.* [17] propose to estimate optical flow in gradient domain by making a gradient consistency assumption. Together with HDR generation, they also try to enhance image resolution through sub-pixel registration. Recently, Hu *et al.* [18] proposed a displacement estimation based method which can deal with large saturated regions in HDR generation by fusing brightness and gradient consistencies on the transformed domain by the intensity mapping function [19].

Another challenge in the HDR generation is the presence of moving objects. Without proper treatments to detect and remove moving objects, ghosting appears in resulting HDR images. Deghosting is a process to detect these outliers which also include saturated and under-exposed regions in LDR images to produce a ghost-free HDR image. Although this problem can be handled with user corrections as demonstrated by Agarwala *et al.* [20], automatic methods are still preferable. Without explicit moving object detection, Khan *et al.* [21] iteratively compute weights to

determine the contribution of different LDR images to the final HDR image with a smaller weight assigned to a pixel that is prone to be an outlier. In [3] and [4], Hasinoff *et al.* and Granados *et al.* respectively define the optimal weights based on noise characteristics to create a noise-free HDR image. Recent work in [5], Gallo *et al.* detect artifact regions explicitly by counting inconsistent pixels in a block-wise comparison, and blend only consistent intensities of LDR images. Raman and Chaudhuri [6] detect artifact regions with similar criteria to the work by Gallo *et al.* [5], but use super-pixel instead of regular patch grid. Heo *et al.* [7] propose a ghost-free HDR imaging framework by using a joint bilateral filter approach. They align LDR images by homographies and detect ghost regions using Graph cuts [22]. Wu *et al.* [23] use criteria such as consistency in the radiance and color across exposures to detect moving objects. Zhang and Cham [24] detect motion by looking for changes in gradients between exposures. Recently, Sen *et al.* [25] propose a patch-based energy-minimization formulation that integrates alignment and reconstruction in a joint optimization through their HDR image synthesis equation. Kalantari *et al.* [26] further extend the work from Sen *et al.* for HDR video generation using alternate exposures. Granados *et al.* [27] analyze noise distribution of color values to reconstruct irradiance from pixels that are likely to correspond to the same static scene object. Lee *et al.* [28] also explore rank minimization in HDR deghosting, but their method cannot handle moving objects with large overlapping area as opposed to our matrix completion algorithm.

There are also hardware based approaches for HDR imaging. Early work in [29], Nayar and Mitsunaga use spatially varying pixel exposures to capture multiple LDR simultaneously for HDR imaging. Unger and Gustavson [30] and Krymski [31] use a rolling shutter with varying exposures. Nayar and Branzoi [32] propose HDR sensors to have a unique response to light for adaptive dynamic range imaging. Wang *et al.* [33] propose a split aperture camera for HDR video capture. Hasinoff *et al.* [34] propose the noise-optimal captures to reduce capturing time of LDR images. Tocci *et al.* [35] develop a versatile HDR video production system using beam splitter. Finally, some new cameras and softwares, such as the Cannon MagicLantern firmware [36], have an HDR video mode that allows for capturing video with alternating ISOs. Although the hardware based approaches have demonstrated impressive HDR imaging, specialized HDR cameras have also been built. These are expensive and are not widely available.

Comparing our work to the aforementioned methods, we exploit the linear dependency of LDR images and formulate the HDR generation problem into a rank minimization problem. A major benefit of our approach is that our formulation allows simultaneously registration and outlier detection of LDR images. Since rank minimization depends only on the sub-space structure of observation matrix and is independent to scale of entries, our method is robust to varying illuminations and magnitude of outliers. As limitations of our approach, we assume the linear camera response function and the scene of input LDR images can be fully aligned by homographies.

3 ALGORITHM

In this section, we formulate HDR generation as a rank minimization problem which simultaneously estimates a set of geometric transformations to align LDR images and detects both moving objects and under/over-exposed regions.

3.1 Low-Rank Structure of Multi-Exposure Images

For a static scene, multi-exposure images taken from a fixed camera are linearly proportional to the exposure time Δt under the linear CRF assumption, when the sensor irradiance R of a scene is constant [13], [37]. While a linear relationship is imposed among the images, we cannot observe the ideal relationship in practice due to artifacts such as camera motions, moving objects, and intensity saturation (as shown in Fig. 1).

We model the forward-intensity acquisition pipeline, called it as IOM, in consideration of the artifacts. In Fig. 1, the artifacts from moving objects do not follow any statistical distribution. Thus, instead of modeling the artifacts using a probabilistic model, we model the artifacts as an additive error e . In addition, we represent the camera motion by a homography transformation group $\mathbf{g} = \{g_1, \dots, g_n\} \in \mathbb{R}^{p \times n}$, which is a p -parameter group. Therefore, the intensity of an image I is observed through the IOM as

$$I = f(k(R + e) \cdot \Delta t) \circ g^{-1}, \quad (1)$$

where f denotes the CRF, \circ denotes a geometric transform operator that transforms an image by geometric transformation $\mathbb{R}^2 \rightarrow \mathbb{R}^2$, and k denotes a camera parameter [13] which depends on focal length of camera lens, diameter of aperture and so on. Since most modern camera lenses are designed to compensate for pixel varying effects, we assume that the parameter k provides a constant mapping between scene radiance and irradiance [2] and is specified by a constant value for each HDR dataset taken by a camera with the same lens, and with fixed focal length and fixed aperture. We also assume the CRF is linear (or calibrated, i.e., $f(I) = I$), because CRF can be readily estimated by various calibration methods. Then, from Eq. (1), each observed image is represented as

$$\begin{aligned} I_i \circ g_i &= f(k(R + e_i) \cdot \Delta t_i) \\ &= kR \cdot \Delta t_i + ke_i \cdot \Delta t_i \quad (f(I) = I) \\ &= A_i + E_i \quad (A_i = kR \cdot \Delta t_i, \\ &\quad E_i = ke_i \cdot \Delta t_i), \end{aligned} \quad (2)$$

where i denotes an image index of multi-exposures.

By stacking the vectorized images I_i , we construct the observation intensity matrix $\mathbf{O} = [\text{vec}(I_1) | \dots | \text{vec}(I_n)] \in \mathbb{R}^{m \times n}$, where m and n are the number of pixels and images, respectively. Similarly, we represent $\mathbf{A} = [\text{vec}(A_1) | \dots | \text{vec}(A_n)]$, $\mathbf{E} = [\text{vec}(E_1) | \dots | \text{vec}(E_n)]$, and $\mathbf{g} = \{g_1, \dots, g_n\} \in \mathbb{R}^{p \times n}$. Thus, we convert the IOM from Eq. (2) into a matrix form $\mathbf{O} \circ \mathbf{g} = \mathbf{A} + \mathbf{E}$, where \circ transforms each vectorized image by each corresponding geometric transformation g . Here, each column of the matrix \mathbf{A} is spanned by sensor irradiance R . This means that the aligned observation $\mathbf{O} \circ \mathbf{g}$ is equal to the latent background irradiance \mathbf{A} , which is the rank-1 matrix, if

there is no artifact in a scene ($\mathbf{E} = \mathbf{0}$). In practice, the rank of $\mathbf{O} \circ \mathbf{g}$ is higher than 1 due to the aforementioned artifacts. Therefore, the robust HDR composition problem becomes a problem to decompose the observation matrix $\mathbf{O} \circ \mathbf{g}$ into the matrix \mathbf{A} close to rank-1 and the error matrix \mathbf{E} while simultaneously estimate the transformations \mathbf{g} that make the matrix \mathbf{A} approaching to rank-1.

3.2 Rank Minimization Approach for aligned images

Our formulation is developed based on the recent advances in Robust Principal Component Analysis (RPCA) [38] by rank minimization to recover a low-rank structure of clean data. The rank of a matrix is independent to the size of a matrix and the magnitude of its entries, but it only depends on the sub-space structure of its entries. Due to this property, the rank minimization based method [38] shows robustness to outliers and optimality from the convexity of the objective function thanks to the blessing of large amounts of data. However, when the number of inputs in \mathbf{O} is very limited, we observed that the solution from [38], [39] includes some outliers as inliers and vice versa. This is because the nuclear norm formulation in [38] not only minimizes the rank of clean data, but it also minimizes the magnitudes of clean data. Such the limited number of observations is common in the HDR problems. In most HDR methods, only 2-5 exposures were captured since the input LDR images already cover almost all the informative dynamic range of a scene. In addition, the magnitudes of radiance in a reconstructed HDR image are usually quite large. Consequently, the method in [38] might not be well suited to the HDR problem.

To derive a better solution, we utilize the prior rank information as a constraint. If the multi-exposure images are already aligned, our problem is formulated into a partial sum objective function as shown in our previous work [10], [11]:

$$\begin{aligned} \mathbf{A}^*, \mathbf{E}^* &= \arg \min_{\mathbf{A}, \mathbf{E}} p_2(\mathbf{A}) + \lambda \|\mathbf{E}\|_1, \\ \text{subject to } \mathbf{O} &= \mathbf{A} + \mathbf{E}, \end{aligned} \quad (3)$$

where $p_2(\mathbf{A}) = \sum_{i=2}^{\min(m,n)} \sigma_i(\mathbf{A})$ is the partial sum of singular values $\sigma_i(\mathbf{A})$ from the second to the last, $\|\cdot\|_1$ denotes l^1 -norm and λ is the weight for sparse error. By using the partial sum instead of the nuclear norm, we encourage the rank-1 constraint rather than enforcing a hard constraint (e.g. by projecting resulting matrix to a low dimensional space).

In practice, we expect that the magnitude of additive error E is proportional to exposure time Δt due to the proportional relationship between E and e in Eq. (2). For example, a moving object affects the images taken with short or long exposure time differently. However, the objective function defined in Eq. (3) treats the error component \mathbf{E} equally which implicitly assumes that the multi-exposure images are affected equally by corrupted radiance from moving objects or saturations. To resolve the problem, we compensate the intensities for each image with exposure time before optimizing Eq. (3). We apply scaling to each input image I_i by the inverse value of i -th exposure time

(e.g. $C \cdot \Delta t_{\text{ref}} / \Delta t_i$, where C is a scaling constant. We set $C = 1$ in the implementation.). After the optimization, the inverse scaling with $\Delta t_i / (C \cdot \Delta t_{\text{ref}})$ is applied to the results to recover the original scale.

3.3 Simultaneous Rank Minimization and Alignment

Rank minimization is not only suitable for outlier detection, but it can also be used in image alignment. In [39], Peng *et al.* showed that batch image alignment task [40] can be performed by enforcing sparsity for outliers and by minimizing rank (nuclear norm, the sum of all the singular values) as similarity cost, instead of using the brightness consistency in conventional alignment methods. Due to the invariant feature of rank to the scale, their alignment results showed robustness to varying illuminations. This formulation is suitable to our model defined in the previous section, as the IOM. Similar to the work in [38], we observe that the alignment method by rank minimization requires a large number of inputs, and could produce a degenerated solution when insufficient inputs are given. Thus, we use the partial sum of singular values instead of nuclear norm in the alignment task which demonstrates better alignment results.

By introducing the geometric parameterization model $\mathbf{O} \circ \mathbf{g} = \mathbf{A} + \mathbf{E}$ to Eq. (3), we can estimate the latent background radiance scene and corrupted regions together with the geometric parameters \mathbf{g} to align the images. The objective function can be defined as follows:

$$\begin{aligned} \mathbf{A}^*, \mathbf{E}^*, \mathbf{g}^* &= \arg \min_{\mathbf{A}, \mathbf{E}, \mathbf{g}} p_2(\mathbf{A}) + \lambda \|\mathbf{E}\|_1, \\ \text{subject to } \mathbf{O} \circ \mathbf{g} &= \mathbf{A} + \mathbf{E}. \end{aligned} \quad (4)$$

Since the constraint including the transformation operator is highly non-linear, it makes the above optimization hard. When the change in \mathbf{g} is small, the constraint can be approximately linearized with current estimate as $\mathbf{O} \circ (\mathbf{g} + \Delta \mathbf{g}) \approx \mathbf{O} \circ \mathbf{g} + \sum_{j=1}^n J_j \Delta \mathbf{g} \epsilon_j \epsilon_j^T$, where $J_i = \frac{\partial}{\partial \zeta} \text{vec}(I_i \circ \zeta)|_{\zeta=g_i} \in \mathbb{R}^{m \times p}$ is the Jacobian of the i -th image with respect to the transformation g_i (we invite readers to [39] for details about the Jacobian representation.) and $\{\epsilon_i\}$ denotes the standard basis for \mathbb{R}^n .

In this work, we assume a small camera motion by hand shake to linearize the transformation operator. We adopt the coarse-to-fine approach on scale pyramid to deal with larger camera motion which cannot be covered by the local approximation. Although the feature based alignments [41] can be applied as initial, and then optimized by our method to achieve the accurate alignment, in this paper, we did not use the feature based method as initial.

3.4 Optimization

The proposed objective functions in Eqs. 3 and 4 form a constrained optimization problem. In recent advances in the rank minimization, Lin *et al.* [42] proposed an augmented Lagrange multipliers (ALM) method [43] to minimize the high dimensional nuclear norm, and Peng *et al.* [39] adopt the ALM method to solve the similar problem of Eq. (4). These approaches are known as scalable and fast convergence. We follow the optimization procedures in [39], [42]

to derive our solution. The proposed Lagrangian function of Eqs. 3 and 4 can be formulated as the following form:

$$\begin{aligned} L(\{\cdot\}, \mathbf{Z}, \mu) &= p_2(\mathbf{A}) + \lambda \|\mathbf{E}\|_1 \\ &\quad + \langle \mathbf{Z}, h(\{\cdot\}) \rangle + \frac{\mu}{2} \|h(\{\cdot\})\|_F^2, \end{aligned} \quad (5)$$

where μ is a positive scalar, $\mathbf{Z} \in \mathbb{R}^{m \times n}$ is an estimate of the Lagrange multiplier matrix, $\langle \cdot, \cdot \rangle$ denotes the matrix inner product, and $\|\cdot\|_F$ denotes the Frobenius norm. We define the constraint function $h(\cdot)$ for each problem respectively as $h(\mathbf{A}, \mathbf{E}) = \mathbf{O} - \mathbf{A} - \mathbf{E}$ for the pre-aligned case defined in Eq. (3) of Sec. 3.2 or $h(\mathbf{A}, \mathbf{E}, \Delta \mathbf{g}) = \mathbf{O} \circ \mathbf{g} + \sum_{j=1}^n J_j \Delta \mathbf{g} \epsilon_j \epsilon_j^T - \mathbf{A} - \mathbf{E}$ for estimating geometric parameter \mathbf{g} simultaneously as defined in Eq. (4) of Sec. 3.3.

To solve Eq. (5), the problem can be divided into three sub-problems for \mathbf{A} , \mathbf{E} , and additionally $\Delta \mathbf{g}$ for the alignment case. The overall solution can be solved by iteratively minimizing the objective functions for \mathbf{A} , \mathbf{E} , and \mathbf{g} until converged. For a simple notation, we denote an auxiliary variable \mathbf{O}'_t as $\mathbf{O}'_t = \mathbf{O}$ for the pre-aligned case of Sec. 3.2 or $\mathbf{O}'_t = \mathbf{O} \circ \mathbf{g} + \sum_{j=1}^n J_j \Delta \mathbf{g}_t \epsilon_j \epsilon_j^T$ for the simultaneous alignment case of Sec. 3.3. We describe the update methods as follows.

Updating A The sub-problem for \mathbf{A} is updated by fixing the other variables, and it is derived by

$$\begin{aligned} \mathbf{A}_{t+1} &= \arg \min_{\mathbf{A}} L(\mathbf{A} | \cdot) \\ &= \arg \min_{\mathbf{A}} p_2(\mathbf{A}) + \langle \mathbf{Z}_t, \mathbf{O}'_t - \mathbf{A} - \mathbf{E}_t \rangle \\ &\quad + \frac{\mu_t}{2} \|\mathbf{O}'_t - \mathbf{A} - \mathbf{E}_t\|_F^2 \\ &= \arg \min_{\mathbf{A}} \mu_t^{-1} \cdot p_2(\mathbf{A}) \\ &\quad + \frac{1}{2} \|\mathbf{A} - (\mathbf{O}'_t - \mathbf{E}_t + \mu_t^{-1} \mathbf{Z}_t)\|_F^2, \end{aligned} \quad (6)$$

where t indicates the iteration index.

Eq. (6) is a rank-1 case in [11], and can be solved by the Partial Singular Value Thresholding (PSVT) operator [11]:

$$\begin{aligned} \mathbb{P}_\tau[\mathbf{Y}] &= \mathbf{U}(\mathbf{D}_{Y1} + \mathcal{S}_\tau[\mathbf{D}_{Y2}])\mathbf{V}^T \\ &= \arg \min_{\mathbf{X}} \frac{1}{2} \|\mathbf{X} - \mathbf{Y}\|_F^2 + \tau \cdot p_2(\mathbf{X}), \end{aligned} \quad (7)$$

where $\mathbf{D}_{Y1} = \text{diag}(\sigma_1, 0, \dots, 0)$,
 $\mathbf{D}_{Y2} = \text{diag}(0, \sigma_2, \dots, \sigma_l)$,

where $\tau > 0$, $l = \min(m, n)$, and $\mathcal{S}_\tau[\mathbf{X}] = \{\text{sign}(x) \cdot \max(0, |x| - \tau)\}$ denotes the entry-wise soft-thresholding operator [44]. \mathbf{U} , \mathbf{V} and \mathbf{D} ($= \mathbf{D}_{Y1} + \mathbf{D}_{Y2}$) correspond to the singular value decomposition of \mathbf{Y} . In Oh *et al.* [11], the PSVT operator provides the closed-form solution of Eq. (7).

For each iteration, \mathbf{A}_{t+1} can be updated with the PSVT operator $\mathbb{P}[\cdot]$ as

$$\mathbf{A}_{t+1} = \mathbb{P}_{\mu_t^{-1}}[\mathbf{O}'_t - \mathbf{E}_t + \mathbf{Z}_t / \mu_t]. \quad (8)$$

Algorithm 1 [RPCA-OURS] RPCA based rank-1 optimization by the ALM.

Input : $\mathbf{O} \in \mathbb{R}^{m \times n}, \mathbf{g} \in \mathbb{R}^{p \times n}, \lambda > 0$.

Initialize $\mathbf{Z}_0, \mathbf{A}_0 = \mathbf{E}_0 = \mathbf{0}, \Delta\mathbf{g}_0 = \mathbf{0}, \mu_0 > 0, \rho > 1$ and $t = 0$.

while not converged **do**

while not converged **do**

$$\mathbf{A}_{t+1} = \mathbb{P}_{\mu_t^{-1}}[\mathbf{O}'_t - \mathbf{E}_t + \mathbf{Z}_t/\mu_t].$$

$$\mathbf{E}_{t+1} = \mathcal{S}_{\lambda\mu_t^{-1}}[(\mathbf{O}'_t - \mathbf{A}_{t+1} + \mu_t^{-1}\mathbf{Z}_t)].$$

For all i ,

$$\Delta g_i^{t+1} = J_i^\dagger \text{vec}(A_{i,t+1} + E_{i,t+1} - O_i \circ g_i - \mu_t^{-1} Z_{i,t}).$$

(only for alignment case).

end while

$$\mathbf{Z}_{t+1} = \mathbf{Z}_t + \mu_t(\mathbf{O}'_{t+1} - \mathbf{A}_{t+1} - \mathbf{E}_{t+1}).$$

$$\mu_{t+1} = \rho\mu_t.$$

end while

Output : $(\mathbf{A}_t, \mathbf{E}_t, \Delta\mathbf{g}_t)$.

Updating \mathbf{E} The sub-problem for \mathbf{E} can be derived by

$$\begin{aligned} \mathbf{E}_{t+1} &= \arg \min_{\mathbf{E}} L(\mathbf{E} | \cdot) \\ &= \arg \min_{\mathbf{E}} \lambda \|\mathbf{E}\|_1 \\ &\quad + \langle \mathbf{Z}_t, \mathbf{O}'_t - \mathbf{A}_t - \mathbf{E} \rangle + \frac{\mu_t}{2} \|\mathbf{O}'_t - \mathbf{A}_t - \mathbf{E}\|_F^2 \\ &= \arg \min_{\mathbf{E}} \lambda \mu_t^{-1} \|\mathbf{E}\|_1 \\ &\quad + \frac{1}{2} \|\mathbf{E} - (\mathbf{O}'_t - \mathbf{A}_t + \mu_t^{-1} \mathbf{Z}_t)\|_F^2. \end{aligned} \quad (9)$$

The form of the objective function in Eq. (9) consisting of the proximity and l^1 -norm terms can be effectively minimized by the soft-thresholding operator $\mathcal{S}_\tau[\cdot]$ defined in [44]. Eq. (9) can be solved by applying the soft-thresholding operator directly:

$$\mathbf{E}_{t+1} = \mathcal{S}_{\lambda\mu_t^{-1}}[\mathbf{O}'_t - \mathbf{A}_{t+1} + \mu_t^{-1} \mathbf{Z}_t]. \quad (10)$$

Updating $\Delta\mathbf{g}$ Solving the sub-problem for $\Delta\mathbf{g}$ is only needed for the simultaneous alignment case. The sub-problem for $\Delta\mathbf{g}$ can be derived from Eq. (5) as

$$\begin{aligned} L(\Delta\mathbf{g} | \cdot) &= \frac{\mu_t}{2} \|\mathbf{O} \circ \mathbf{g} + \sum_{j=1}^n J_j \Delta\mathbf{g} \epsilon_j \epsilon_j^T - \mathbf{A}_t - \mathbf{E}_t + \mu_t^{-1} \mathbf{Z}_t\|_F^2. \end{aligned} \quad (11)$$

Since Eq. (11) is a quadratic equation for the variable $\Delta\mathbf{g}$, it can be solved in a least square sense. The closed-form solution of Δg_i is updated by the following equation.

$$\Delta g_i^{t+1} = J_i^\dagger \text{vec}(A_{i,t} + E_{i,t} - O_i \circ g_i - \mu_t^{-1} Z_{i,t}), \quad (12)$$

where the sub-index notation i denotes the i -th column vector (the i -th image) of the matrix, J_i^\dagger denotes the Moore-Penrose pseudo-inverse of J_i .

Updating \mathbf{Z} The update strategy of the Lagrange multiplier \mathbf{Z} follows the basic strategy of the ALM method [42], [43], [45] as the following equation:

$$\mathbf{Z}_{t+1} = \mathbf{Z}_t + \mu_t \cdot h(\{\cdot\}). \quad (13)$$

Overall Procedures The algorithm to solve Eq. (5) is summarized as Alg. 1. During the inner loop in optimization,

the sub-problems are optimized until converged. In our experiments, we found that optimizing the inner loop once is enough to converge a correct solution and shows faster convergence behavior.

Due to the linearization of transformation, Alg. 1 is only valid for local changes on $\Delta\mathbf{g}$. To avoid local minima, Alg. 1 proceeds iteratively in a coarse-to-fine manner. We adopt explicit warping with current optimized geometric parameters after each convergence of Alg. 1. The algorithm is terminated when the iteration and explicit warping is converged at the finest scale. Fig. 2-(a) and (b) shows our intermediate results where input images are automatically aligned and decomposed into low-rank LDR images and sparse outlier images.

3.5 Extension to Matrix Completion

As noted by Srikantha and Sidibé [46] in a recent review on the ghost detection and removal for HDR imaging, “there is no single best method and the selection of an approach depends on the user’s goal”. It is necessary to allow user control in the HDR deghosting problem where a simple solution to remove all outlier moving objects may not be a preferable solution. In addition, in the presence of large moving objects but with small movements, parts of the moving objects may appear across every LDR images. In such cases, our outlier rejection method would remove the parts that were not overlapped, but the overlapping parts would remain in the reconstructed HDR image as a biased low-rank component. This causes a failure in our method. Similarly, if more than half of LDR images have the same saturated regions, the outlier rejection method can consider the saturated regions as inliers and rejects the correct image details as outliers.

In this subsection, we further reformulate our problem into a low-rank matrix completion (MC) problem where a user is allowed to select preferable moving objects or regions which will be left in the final HDR image. By discarding the entries of coefficient selected by a user, the matrix completion repairs the low-rank components in other LDR images by properly re-scaling the fixed entries to match the exposure time of other LDR images. This allows us to produce a set of pseudo LDR images where moving objects are well-aligned and consistent with background exposure.

Given the fixed locations of user selected entries (This can be achieved using the method in [20] with simple user mark-ups and segmentation), our goal is to recover a low-rank matrix, essentially a rank-1 matrix, with missing entries (user selected regions in other LDR images or saturated regions) and unknown corruptions (non-selected regions). This shares the same spirit with the MC problem [47], [48]. The MC problem with our partial sum of singular values can be formulated as:

$$\min_{\mathbf{A}, \mathbf{E}} p_2(\mathbf{A}) + \lambda \|\mathbf{E}\|_1 \quad \text{s.t.} \quad \mathcal{P}_\Omega(\mathbf{O}) = \mathcal{P}_\Omega(\mathbf{A} + \mathbf{E}), \quad (14)$$

where $\mathcal{P}_\Omega(\cdot) : \mathbb{R}^{m \times n} \rightarrow \mathbb{R}^{m \times n}$ is an orthogonal projection operator which defines over valid entries, Ω , of observations. In other words, we are considering the following

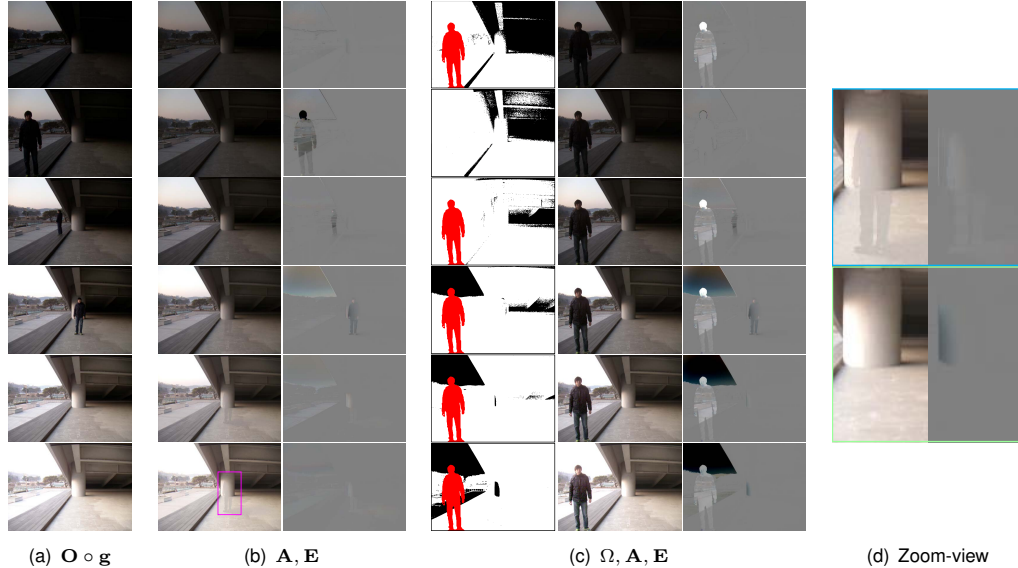


Fig. 2: Intermediate results after rank minimization. (a) Aligned $\mathbf{O} \circ \mathbf{g}$, (b) Low-rank \mathbf{A} and sparse outlier \mathbf{E} obtained by *RPCA-OEURS* (c) Ω (red masks are provided by user, and black regions are automatically detected saturation/under-exposed regions), low-rank \mathbf{A} and sparse outlier \mathbf{E} obtained by *MC-OEURS*. An offset, 0.5, is added to \mathbf{E} for display purpose. (d) Comparison between *RPCA-OEURS* (Top) and *MC-OEURS* (Bottom). Since *MC-OEURS* excluded the saturation regions as missing values, the estimated low rank matrix is more accurate. While the results in *RPCA-OEURS* are biased by the large saturation region that appears consistently across half number of input images.

problem:

$$\mathbf{O}_{ij} = \begin{cases} A_{ij} + E_{ij}, & \forall(i, j) \in \Omega \\ \emptyset, & \forall(i, j) \in \Omega^c \end{cases}$$

where \emptyset is an empty set which represents missing values in the observations.

Again, the optimization problem can be formulated by the ALM as follow:

$$L(\mathbf{A}, \mathbf{E}, \mathbf{Z}, \mu) = p_2(\mathbf{A}) + \lambda \|\mathcal{P}_\Omega(\mathbf{E})\|_1 + \langle \mathbf{Z}, \mathcal{P}_\Omega(\mathbf{O} - \mathbf{A} - \mathbf{E}) \rangle + \frac{\mu}{2} \|\mathcal{P}_\Omega(\mathbf{O} - \mathbf{A} - \mathbf{E})\|_F^2. \quad (15)$$

We now describe the optimization procedures for Eq. (15), by splitting the problem into the sub-problems for \mathbf{A} and \mathbf{E} . The significant difference is on optimizing \mathbf{A} , which can be formulated as:

$$\begin{aligned} \mathbf{A}_{t+1} &= \arg \min_{\mathbf{A}} p_2(\mathbf{A}) + \langle \mathbf{Z}_t, \mathcal{P}_\Omega(\mathbf{O} - \mathbf{A} - \mathbf{E}_t) \rangle \\ &\quad + \frac{\mu_t}{2} \|\mathcal{P}_\Omega(\mathbf{O} - \mathbf{A} - \mathbf{E}_t)\|_F^2 \\ &= \arg \min_{\mathbf{A}} \mu_t^{-1} p_2(\mathbf{A}) \\ &\quad + \frac{1}{2} \|\mathcal{P}_\Omega(\mathbf{A}) - (\mathcal{P}_\Omega(\mathbf{O} - \mathbf{E}_t) + \mu_t^{-1} \mathbf{Z}_t)\|_F^2. \end{aligned} \quad (16)$$

In contrast to Eq. (8), Eq. (16) cannot be solved in a closed-form manner due to the projection operator. Therefore, we solve it iteratively. This process is inspired by the Accelerated Proximal Gradient (APG) approach [49], [50]. The iterative procedures can be summarized as:

- 1) $\mathbf{Q}_k = \mathbf{A}_{t,k} + \frac{b_k - 1}{b_{k+1}} (\mathbf{A}_{t,k} - \mathbf{A}_{t,k-1})$,
- 2) $\mathbf{A}_{t,k+1} = \mathbb{P}_{\mu_t^{-1}} [\mathcal{P}_\Omega(\mathbf{O} - \mathbf{E}_t) + \mathcal{P}_{\Omega^c}(\mathbf{Q}_k) + \mathbf{Z}_t / \mu_t]$,
- 3) $b_{k+1} = \frac{1 + \sqrt{1 + 4b_k^2}}{2}$,
- 4) After converged, $\mathbf{A}_{t+1} = \mathbf{A}_{t,k+1}$,

where b_i is a positive sequence with the initial $b_0 = 1$.

Solving the sub-problem for \mathbf{E} is similar with Eqs. 9 and (10) as follows.

$$\begin{aligned} \mathcal{P}_\Omega(\mathbf{E}_{t+1}) &= \arg \min_{\mathcal{P}_\Omega(\mathbf{E})} \lambda \|\mathcal{P}_\Omega(\mathbf{E})\|_1 + \langle \mathbf{Z}_t, \mathcal{P}_\Omega(\mathbf{O} - \mathbf{A}_t - \mathbf{E}) \rangle \\ &\quad + \frac{\mu_t}{2} \|\mathcal{P}_\Omega(\mathbf{O} - \mathbf{A}_t - \mathbf{E})\|_F^2 \\ &= \arg \min_{\mathcal{P}_\Omega(\mathbf{E})} \lambda \mu_t^{-1} \|\mathcal{P}_\Omega(\mathbf{E})\|_1 \\ &\quad + \frac{1}{2} \|\mathcal{P}_\Omega(\mathbf{E}) - \mathcal{P}_\Omega(\mathbf{O} - \mathbf{A}_t) - \mu_t^{-1} \mathbf{Z}_t\|_F^2, \end{aligned} \quad (17)$$

and its corresponding closed-form solution is defined as:

$$\mathcal{P}_\Omega(\mathbf{E}_{t+1}) = \mathcal{S}_{\lambda \mu_t^{-1}} [\mathcal{P}_\Omega(\mathbf{O} - \mathbf{A}_t) + \mu_t^{-1} \mathbf{Z}_t]. \quad (18)$$

After converged, we re-estimate $\mathbf{E} = \mathbf{O} - \mathbf{A}$ to obtain all values of \mathbf{E} including the missing entries. Alg. 2 summarizes the optimization procedures. Similar to the rank minimization formulation, we can include geometric alignment in the MC formulation. However, we omit it for the clarity of presentation since the additional procedures are similar.

Compared to previous methods, especially the method in Agarwala *et al.* [20], our MC solution can accurately correct the exposure of selected moving objects in different exposure setting of LDR images. This allows the reconstructed HDR image to have the correct exposure for the selected moving objects while the method in [20] does not correct exposure of moving objects. Compared to the recent methods in Sen *et al.* [25], Hu *et al.* [18], and Kalantari *et al.* [26] where they also reconstruct pseudo LDR images before the HDR image reconstruction, our MC solution cannot recover the dynamic range of moving HDR objects. Essentially, the details of moving objects are likely to be reconstructed from a single image. However, since we do not find patch-wise correspondences as performed in [18], [25], our approach can avoid discontinuities and misalignment artifacts due to mismatches of patches. Note that accurate matching of moving objects with large movement

Algorithm 2 [MC-OURLS] Rank-1 matrix completion by the ALM.

Input : $\mathbf{O} \in \mathbb{R}^{m \times n}, \Omega = \{0, 1\}^{m \times n}, \lambda > 0.$

 Initialize $\mathbf{A}_0 = \mathbf{O}, \mathbf{E}_0 = \mathbf{Z}_0 = \mathbf{0}, \mu_0 > 0, \rho > 1$ and $t = 0$.
while not converged **do**
while not converged **do**
 $b_0 = 1, \mathbf{Q}_0 = \mathbf{A}_t, \mathbf{A}_{t,0} = \mathbf{A}_t$
while not converged **do**

$$\mathbf{A}_{t,k+1} = \mathbb{P}_{\mu_t^{-1}}[\mathcal{P}_\Omega(\mathbf{O} - \mathbf{E}_t) + \mathcal{P}_{\Omega^c}(\mathbf{Q}_k) + \frac{1}{\mu_t} \mathbf{Z}_t]$$

$$b_{k+1} = \frac{1 + \sqrt{1 + 4b_k^2}}{2},$$

$$\mathbf{Q}_{k+1} = \mathbf{A}_{t,k+1} + \frac{b_{k+1}}{b_{k+1}} (\mathbf{A}_{t,k+1} - \mathbf{A}_{t,k}),$$

end while

$$\mathbf{A}_{t+1} = \mathbf{A}_{t,k+1}.$$

$$\mathcal{P}_\Omega(\mathbf{E}_{t+1}) = \mathcal{S}_{\lambda \mu_t^{-1}}[\mathcal{P}_\Omega(\mathbf{O}_t - \mathbf{A}_{t+1}) + \mu_t^{-1} \mathbf{Z}_t].$$

end while

$$\mathbf{Z}_{t+1} = \mathbf{Z}_t + \mu_t (\mathcal{P}_\Omega(\mathbf{O}_{t+1} - \mathbf{A}_{t+1} - \mathbf{E}_{t+1})).$$

$$\mu_{t+1} = \rho \mu_t.$$

end while

$$\mathbf{E}_t = \mathbf{O} - \mathbf{A}_t.$$

Output : $(\mathbf{A}_t, \mathbf{E}_t).$

is an ill-posed problem especially if the shape of moving objects can be deformed. Compared to Granados *et al.* [27], their approach requires noisy inputs since their exposure correction is relied on matching noise statistics under different exposures. Consequentially, their reconstructed HDR images can be noisy. On the other hand, our approach does not have this requirement on inputs. In Fig. 2-(c), we show the intermediate results after MC. More discussions on the results between our two methods in Alg. 1 and Alg. 2 will be provided in Sec. 4.2.2.

3.6 Implementation

This subsection provides additional implementation details needed to reproduce our results. Across all experiments, we set $\lambda = 1/\sqrt{\max(m, n)}$ in Eqs. 3, 4 and 14, where m and n are the row and column size of the matrix \mathbf{O} ; therefore there is no manual tuning parameter.

Radiometric calibration In many cameras, nonlinearity between sensor irradiance and image intensity is intentionally programmed by camera manufacturers. However, our rank minimization methods assume a linear CRF $f(\cdot)$. Thus, the radiometric calibration step is necessary if the camera CRF is nonlinear. In our experiments, we utilize the method in Lee *et al.* [37] which is one of the state-of-the-art method to estimate CRF from input images captured with different exposure. Once $f(\cdot)$ is estimated, $f^{-1}(I)$ is applied on the image intensity I to linearize the inputs.

Saturation and under-exposure assessment When a region is over-exposed/under-exposed, the rank-1 linear relationship is violated. In our MC formulation, we can consider them as missing values and then repair the missing entries using Alg. 2. To detect the outlier regions, we masked out extreme intensity values as follow:

$$M^i(I) = \begin{cases} 1, & I_{th} < I^i < 1 - I_{th}, \\ 0, & \text{otherwise,} \end{cases} \quad (19)$$



Fig. 3: Our user input for MC-OURLS. (a) Automatic method through outlier analysis, (b) User mark-up on super-pixel segmentation [52].

where M^i is a saturation mask for the i -th LDR images, I_{th} denotes the saturation threshold value which is set to 2/255 in our implementation. This process is applied to RGB channels individually.

HDR composition and tone mapping To composite an HDR image from repaired low-rank LDR images, we follow the standard method in [2]:

$$H(x) = \frac{1}{n} \sum_{i=1}^n A^i(x)/\Delta t_i, \quad (20)$$

where n represents the number of input images, and $H(x)$ and $A^i(x)$ denote an estimated radiance and a low-rank intensity respectively.

After the HDR composition, we apply the tone-mapping using the local adaptation method in Photoshop CS6 to convert HDR to LDR. This is the same representation as in Sen *et al.* [25], where the results are manually tone-mapped by Photomatix [51]. In experimental comparisons, we manually tune the tone-mapping parameters to match our results with the results from Sen *et al.* [25]. In comparisons with results from Heo *et al.* [7], we use the executables provided by the author to produce their tone-mapped HDR images.

User input for matrix completion We provide two methods to mark up outlier masks for moving objects inclusion in our MC-OURLS formulation. In the first case where moving objects are non-overlapping, we can identify the moving objects in the sparse outlier \mathbf{E} after RPCA-OURLS as illustrated in Fig. 3 (a). This method is used to produce our results in Figs. 2, 13, 14, and 15 respectively. In the case where moving objects are overlapped, we provide a simple user interface which allows a user to mark on super-pixels of a reference image to indicate outlier masks of other images as illustrated in Fig. 3 (b). This method is used to produce our results in Fig. 17. In Fig. 18, we first use the first method to make an initial mask, and then use the second method to correct the mask of the acrobat.

Computational time Our methods are implemented on Matlab without any code optimization. To compare running time with other algorithms, we perform an experiment on a PC with i7-2600 (3.4GHz) and 24 Gb RAM with 5 input images with 640×480 size. For our method with alignment, we use 3 scale pyramid levels. Below shows our running time and comparisons of running time with three state-of-the-art HDR algorithms, i.e. Heo [7], Hu [18], and Sen [25].

	Heo [7]	Hu [18]	Sen [25]	RPCA-OURLS	RPCA-OURLS +Align	MC-OURLS
Env.	C++	Matlab +Mex	Matlab +Mex	Matlab	Matlab	Matlab
Run time	3 min	94 s	106 s	10 s	57 s	144 s

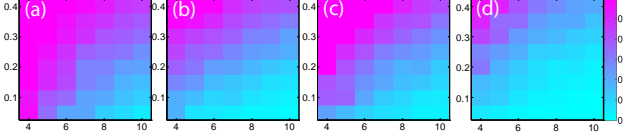


Fig. 4: Reconstruction error for synthetic data with varying numbers of columns n . (a) *RPCA*. (b) *RPCA-Ours*. (c) *MC*. (d) *MC-Ours*. The Y-axis represents the corruption ratio $r \in [0, 0.4]$. The X-axis represents the column size $n \in [4, 10]$ for the rank-1 case. The color magnitude represents the normalized reconstruction error $\frac{\|\mathbf{A}_{GT} - \hat{\mathbf{A}}\|}{\|\mathbf{A}_{GT}\|}$.

4 EXPERIMENTAL RESULTS

To evaluate the proposed algorithm, we systematically analyze the performance using synthetic examples and then compare our results with results from the state-of-the-art HDR algorithms using challenging real world examples. In the following subsections, we present evaluation results for alignment, HDR background (latent) image decomposition, and HDR composition.

4.1 Synthetic Evaluations

We provide synthetic evaluations for our core algorithms, which are the rank minimization methods based on RPCA and MC. To synthesize a ground-truth low-rank (rank 1) matrix $\mathbf{A}_{GT} \in \mathbb{R}^{m \times n}$, we perform a linear combination of a arbitrary orthogonal basis vector with a weight vector to span each column vector. The weight vector is randomly sampled from the uniform distribution $U[0, 1]$. To generate sparse outliers, we select $m \times n \times r$ entries from \mathbf{A}_{GT} , where r denotes the corruption ratio. Larger r means more outlier entries. The selected entries are corrupted by random errors from $U[0, 1]$. We ran each of the following tests, over 30 trials, and report the averages of overall trials.

We denote the proposed models as *RPCA-Ours* for Eq. (3) and *MC-Ours* for Eq. (14), and *RPCA* for [38] (the nuclear norm based RPCA) and *MC* for [53] (the nuclear norm based MC).

4.1.1 Recoverability

To verify the robustness of our methods against outliers, we measure the average error between the ground-truth and the recovered $\hat{\mathbf{A}}$ as $\frac{\|\mathbf{A}_{GT} - \hat{\mathbf{A}}\|}{\|\mathbf{A}_{GT}\|}$. We vary the column size n (*i.e.* the number of observations) according to corruption ratio, and we fixed the row $m = 10,000$. For the MC methods, we remove 30% of outlier as missing entries to recover $\hat{\mathbf{A}}$. The missing entries mimic saturated regions in LDR images.

The results are shown in Fig. 4. The larger the blue area, the more robust the tested algorithms. As n decreases (*i.e.* the number of observations decreases), the recoverability of the conventional RPCA based methods in (a,c) decrease, while our methods in (b,d) still have larger recoverable area.

We have also quantitatively evaluated the performance on a more realistic data. We generate synthetic LDR images with linear CRF and no geometric misalignment. The ground truth HDR images are obtained from the sIBL archive [54]. We add 5% additive random noise to the LDR images. Fig. 5 show the comparison between *RPCA* and *RPCA-Ours*. Our method shows better PSNR than *RPCA*.

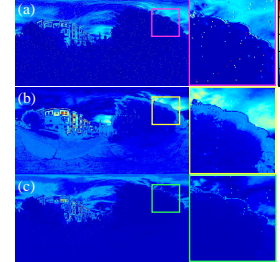


Fig. 5: Quantitative results for denoising. Top: Test examples. Middle: PSNR. Bottom: An example error maps for *Street* data between (a) Photoshop CS6, (b) the conventional *RPCA* and (c) *Ours*. The error maps show the normalized absolute error $AE = |H_{GT}(x) - H_{est}(x)|$.

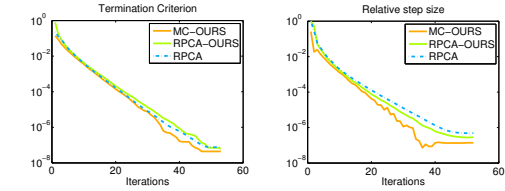


Fig. 6: Convergence. (Left) Termination criterion according to outer iterations. (Right) Relative step size ($\frac{\|\mathbf{A}_t - \mathbf{A}_{t-1}\|}{\|\mathbf{A}_t\|}$) according to outer iterations.

on most of the tested examples. We have also compare the performance with Photoshop CS6 which has a built-in ghost removal function. The error map in Figs. 5-(a-c) show the absolute error $AE = |H_{GT}(x) - H_{est}(x)|$ for the green channel, where H_{GT} and H_{est} are the ground truth HDR and the restored HDR images respectively. Comparing the results, both *RPCA* and *RPCA-Ours* shows better denoising than Photoshop CS6 in the magnified view. Our method grossly shows the least error in Fig. 5-(c). The *RPCA* fails to recover scene radiance especially for large radiance regions due to limited observations, and the nuclear norm favors a solution with smaller magnitudes. More results can be found in the supplementary material, which can be found on the Computer Society Digital Library at <http://doi.ieeecomputersociety.org/10.1109/TPAMI.2014.2361338>.

4.1.2 Convergence

To examine the convergence behavior of both *RPCA-Ours* and *MC-Ours*, we plot the evolution of the relative step size $\frac{\|\mathbf{A}_t - \mathbf{A}_{t-1}\|}{\|\mathbf{A}_t\|}$ and termination criteria $\frac{\|\mathbf{O} - \mathbf{A} - \mathbf{E}\|_F}{\|\mathbf{O}\|_F}$ over the outer iterations in Fig. 6. We randomly generated rank-1 matrices with $m = 10,000$ rows and $n = 10$ columns, and the average values over the trials are reported.

Fig. 6 shows gradual convergence under the same termination criterion. The fluctuation in the relative step size results in (Right) near the iteration 35 is due to early termination of a few trials. In an individual trial, the relative step size are typically monotonically decreasing. In our real world experience, our algorithms converge for all testing examples.

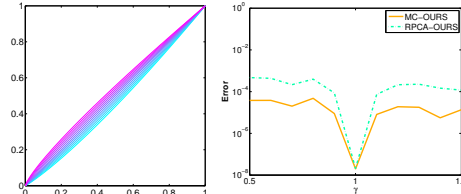


Fig. 7: Left: Synthetically generated weak nonlinear response functions. Right: Reconstruction error $\frac{\|A_{GT} - \hat{A}\|}{\|A_{GT}\|}$ against degree of nonlinearity controlled by γ .



Fig. 8: Comparisons of our results with and without the radiometric calibration. One of input images (Left). The low-rank latent images without (Middle) and with (Right) CRF correction.

4.1.3 Effects of CRF

When a CRF is nonlinear, we apply the method in [37] to calibrate CRF and then linearize our inputs. However, because of imperfect estimation, weak nonlinearity can remain. We evaluate the effects of remaining weak nonlinearity using synthetically generated weak nonlinear response functions as shown in Fig. 7-(Left). The weak nonlinear functions are generated by combining a linear function and a gamma curve as $f(x) = \gamma \cdot x + (1 - \gamma) \cdot x^{1.5}$ for $0 \leq \gamma \leq 1$, and $f(x) = \alpha \cdot x + (1 - \alpha) \cdot x^{\frac{1}{1.5}}$ for $1 < \gamma \leq 2$, where $\alpha = 2 - \gamma$. Fig. 7-(Right) shows the error $\frac{\|A_{GT} - \hat{A}\|}{\|A_{GT}\|}$ according to different nonlinearity parameter. As expected, our algorithms perform better with better linearized inputs. Fig. 8 shows comparisons on reconstructed HDR images with and without CRF correction. The results are obtained using RPCA-OURS. Weak ghosting artifacts appear in the results without CRF correction. Thus, to achieve high quality results, preprocessing with CRF correction is a necessary.

4.2 Real world examples

4.2.1 Alignment among Different Exposures

We first validate the performance of our alignment algorithm. Since common image alignment methods follow the brightness consistency assumption [40], this assumption is no longer valid in our HDR scenario. We compare accuracy of our alignment algorithm to RASL [39], which is a state-of-the-art alignment algorithm that is also based on RPCA.

In our experiment, we use the *SculptureGarden* dataset which contains large area of saturations and under-exposed regions, as well as moving objects. We synthetically generate misaligned images by applying affine transformation randomly and then evaluate the performance of registration. The random affine transformation is defined as $[a_{11} \ a_{12} \ a_{13}; a_{21} \ a_{22} \ a_{23}; 0 \ 0 \ 1]$ (where $a_{\{11,22\}} \sim \mathcal{N}(1, 0.05^2)$, $a_{\{12,21\}} \sim \mathcal{N}(0, 0.05^2)$, and $a_{\{13,23\}} \sim \mathcal{N}(0, \sigma^2)$). Fig. 9 and 10 show the registration results¹. Again, our approach achieves high accuracy in registration as shown in the



Fig. 9: An example of unaligned input and our output (RPCA-OURS) on the *SculptureGarden* dataset.

σ	1	2	4	8	16	24
Ours	0.11	0.11	0.10	0.11	0.11	0.13
RASL	119.54	80.34	99.86	68.30	101.41	116.99
F. Init	0.82	1.07	1.11	1.03	0.86	1.31
F.+Bundle	0.32	0.40	0.42	0.36	0.37	0.42

Fig. 10: Quantitative comparisons of alignment accuracy on the *SculptureGarden* dataset. Misaligned inputs are synthetically generated using random affine transforms. The average alignment errors over 5 trials are reported.



Fig. 11: An alignment result on a real world example. Left: Average of unaligned inputs, Middle: Alignment results by Zimmer et al. [17], Right: Our alignment results.

RMSE in Fig. 10. We have also provide the comparisons with sparse feature matching based method [41] denoted as F. Init (before global nonlinear optimization) and F. Bundle (after global nonlinear optimization). We note that RASL shows unnaturally large errors in the experiments. Upon careful investigation, we found that results in RASL were biased by the large saturation regions where RASL tried to find the transformation that minimize the effects of the saturated regions by shrinking the area of saturated regions. As discussed previously, the nuclear norm solution in RPCA not only try to find a low-rank solution, but it also try to find a solution that minimizes the magnitude of entries in the recovered low-rank matrix. This problem is more significant when there is limited number of observations which caused the bias in their estimation. In contrast, our approach does not have this bias. Comparing to F.+Bundle, our approach achieves lower RMSE, since our measurement is per-pixel based.

We show an alignment result on a real world example in Fig. 11. The input images are from Zimmer et al. [17]. Our alignment is accurate and robust to illumination changes. Compared to the pixelwise optical flow alignment by Zimmer et al., our method utilizes a parametric transformation. Thus, if the camera movement violates our model, our alignment may contain blurriness as illustrated in the sky region in Fig. 11 (Bottom). In contrast, if our model assumption is satisfied, our registration result will be better than Zimmer et al. as illustrated in Fig. 11 (Top). Note that our alignment within the building region in Fig. 11 (Bottom) is also more accurate than the alignment by Zimmer et al. as shown in the zoom-in regions.

1. We provide intermediate alignment results for the $\sigma = 2$ case at here: <http://thoh.kaist.ac.kr/research/partialsum/hdr/align.gif>



Fig. 13: Comparison of HDR results with other methods on the *Arch* dataset [5]. (a) Debevec and Malik [2]. (b) Mertens *et al.* [55]. (c) Gallo *et al.* [5]. (d) Photoshop CS6. (e) Heo *et al.* [7]. (f) Hu *et al.* [18]. (g) Sen *et al.* [25]. (h) Lee *et al.* [28]. (i) Ours (*MC-OOURS*). Error regions are highlighted. No user input is required for this example.

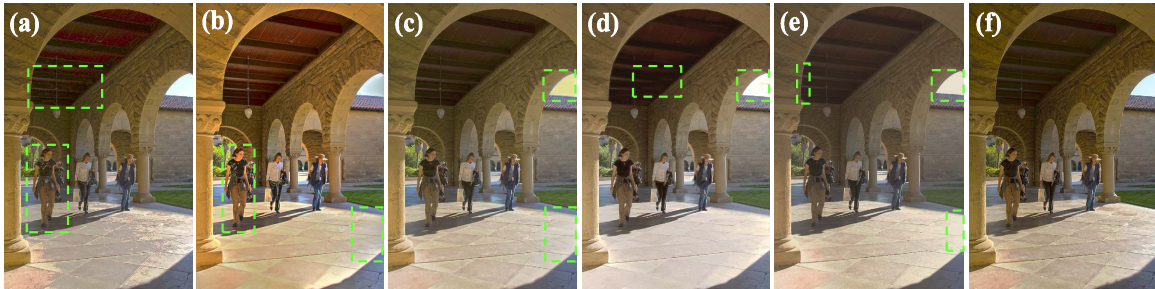


Fig. 14: Comparison of HDR results with other methods on *Arch* dataset [5]. (a) Photoshop CS6. (b) Heo *et al.* [7]. (c) Hu *et al.* [18]. (d) Sen *et al.* [25]. (e) Lee *et al.* [28]. (f) Ours (*MC-OOURS*). Mertens *et al.* [55] and Gallo *et al.* [5] do not have results for moving objects inclusion. Error regions are highlighted.

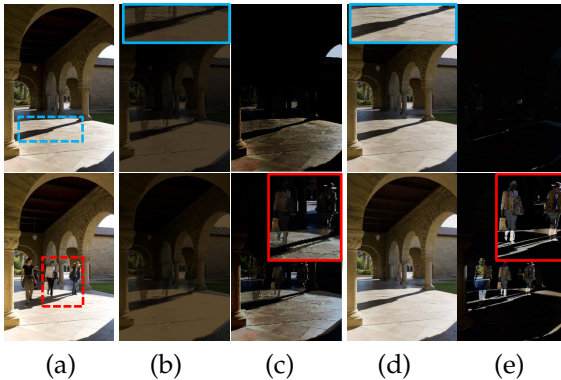


Fig. 12: Comparisons of decomposition results to latent background \mathbf{A} and outliers \mathbf{E} from RPCA [38] and our method (*RPCA-OOURS*). (a) Two sampled input images. (b,c) Low-rank \mathbf{A} and sparse outlier \mathbf{E} obtained by RPCA. (d,e) Low-rank \mathbf{A} and sparse outlier \mathbf{E} obtained by our method. Absolute magnitude of \mathbf{E} is shown.

4.2.2 Background Decomposition

We evaluate the accuracy of background modeling to reject outliers caused by moving objects. In this evaluation, the input LDR images are well aligned. We compare our method (*RPCA-OOURS*) with *RPCA* [38] which minimizes nuclear

norm to decompose low-rank background and sparse outlier moving objects. The *Arch* dataset [5] is used in this evaluation, and the decomposition results are reported in Fig. 12. Ideally, the decomposed background (low-rank matrix \mathbf{A} 's) in (b) and (d) should have similar intensities with inputs in (a) where moving objects or saturated regions are removed. However, the decomposition results by *RPCA* show darker background because nuclear norm implicitly favors a solution with smaller magnitude, and there are not enough input images to support large magnitude. In comparisons, our result does not have this problem and can correctly separate background and moving objects.

We provide self-comparison between *RPCA-OOURS* and *MC-OOURS* in Fig. 2. Our results in *MC-OOURS* is more accurate because it explicitly handles saturations as missing values. While our results in *RPCA-OOURS* are biased by the large saturated regions which covers half number of input images. The saturation regions violate the sparsity assumption which causes errors in *RPCA-OOURS*. With user specified masks (Red masks), *MC-OOURS* can also be used to include moving objects explicitly in the recovered low-rank matrix. If sparsity assumption about moving objects and saturations are satisfied, and there is no user specified mask,



Fig. 15: Comparison of HDR results with Photoshop CS6. Left: Photoshop CS6, Right: our results (*MC-OEURS*, no user mark-up). Top: Sampled input LDR images out of 6 input images.

the results from *RPCA-OEURS* and *MC-OEURS* are almost identical.

4.2.3 HDR Reconstruction

We evaluate and qualitatively compare our HDR results with results from previous methods. In Fig. 13, our result is compared with Debevec *et al.* [2], Mertens *et al.* [55], Gallo *et al.* [5], Photoshop CS6, Heo *et al.* [7], Hu *et al.* [18], and Sen *et al.* [25]. The *Arch* dataset [5] is used for comparisons. Our result is generated using *MC-OEURS* algorithm without user markups. As shown in Fig. 13, ghost-artifacts appear in the results of both Debevec and Malik [2] and Mertens *et al.* [55] algorithms since their algorithms were not designed to handle moving objects. The results in other algorithms can successfully remove ghosting from moving objects. However, as noted in the highlighted regions, the results of Gallo *et al.* [5] and Photoshop CS6 contain blending artifacts. The result of Heo *et al.* [7] has halo artifacts. The results of Hu *et al.* [18] and Sen *et al.* [25] contain patches misalignment artifacts especially in the dark regions. In contrast, our result does not have the aforementioned artifacts. Note that no user input is required to produce our result in this example.

We further compare the results with moving objects inclusion in Fig. 14 using the same *Arch* dataset [5]. In this example, our moving object mask is detected automatically by using the detected outlier regions (excluding saturation and under-exposed regions) in the fourth reference images as described in Sec. 3.6. The result from Heo *et al.* [7] appears to have ghost artifacts in the included moving objects (background texture appears in the moving objects). The result from Sen *et al.* [25] performs well in moving objects inclusion, but shows artifacts in dark regions due to mismatch of patches. We additionally compare the performance of our method and Photoshop CS6 on a real world dataset captured by ourselves in Fig. 15. Serious artifacts appear in the results from Photoshop CS6.

We have also further compare our results with results from Sen *et al.* [25] and Hu *et al.* [18] in Figs. 16 and 17. They are regarded as the recent state-of-the-art methods specifically designed for moving objects handling in HDR reconstruction. Both methods are based on patch matching to enhance HDR reconstruction of moving objects since global transformation cannot perform well to match moving objects. As shown in Fig. 16, when there are mismatches, especially for regions that are challenging for local patch matching, artifacts are produced as shown in the result

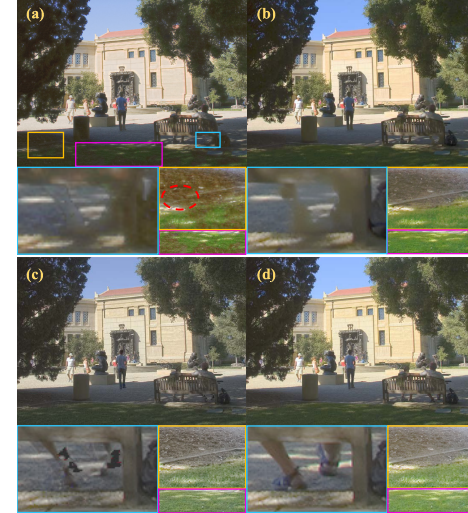


Fig. 16: Comparison of HDR result on the *SculptureGarden* dataset [5] with (a) Sen *et al.* [25], (b) Hu *et al.* [18], (c) Lee *et al.* [28] and (d) our method (No user mark-up.). The same tone-mapping is applied. In zoom-in views, we increased contrast by 30 percents for better visualization.

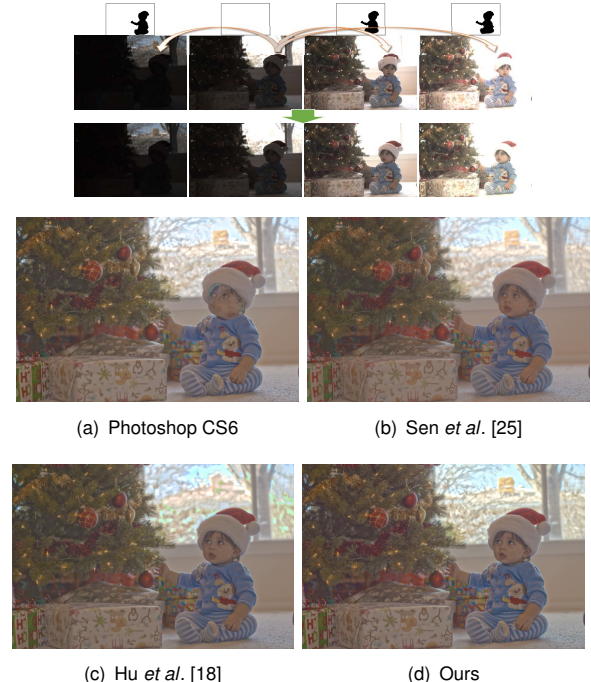


Fig. 17: *SantasLittleHelper* [25]. (Top) Illustration of our MC approach in this example. Four pseudo LDR results out of seven are shown. (Bottom) Reconstructed HDR images. Although our method reconstructs details of the moving object from a single LDR image, the quality is as good as the results from Sen *et al.* and Hu *et al.* that apply patch matching to merge details of the moving object from different LDR images. The amount of user inputs for our result are described in Sec. 3.6.

of Sen *et al.* The results of Hu *et al.* are more stable, but we also observe color degradation due to mismatch on saturation region as shown in Fig. 17. In comparison, although our approach uses details from a single image to recover HDR image of moving objects using matrix completion, our recovered details within the moving objects are as good as the results from Sen *et al.* and Hu *et al.* as shown in Fig. 17. However, our approach can effectively eliminate the possibility of mismatch artifacts. For reference, we also show our reconstructed pseudo LDR images using the example provided by Sen *et al.* in Figs. 17.

Finally, we compare our result with a result from Grana-



Fig. 18: Acrobat [27]. (a) Granados *et al.* [27]. (b) Lee *et al.* [28]. (c) Ours (MC-OEURS). Top Right: 3 input LDR images are shown. The red box region is enlarged for comparison. (d-g) Zoomed-in view of an input LDR image and the results of the three compared methods in same order. The amount of user inputs for our result are described in Sec. 3.6.

dos *et al.* [27] in Fig. 18. The work from Granados *et al.* is designed to handle ghosting in HDR reconstruction. Instead of using patch match, Granados *et al.* use noise statistics to match regions across different dynamic range to composite an HDR image. We apologize that we cannot provide comparisons with results from Granados *et al.* in the previous examples since we do not have their executable. As shown in Fig. 18, our approach demonstrates a high quality HDR reconstruction that is as good as the result from Granados *et al.* Because user control is allowed, our approach can produce the result that is more semantically accurate such as the shadow region shown in Fig. 18-(e,g).

5 CONCLUSION

In this paper, we have presented a rank minimization framework for the HDR reconstruction problem. Our approach is based on the rank-1 structure of LDR images derived from image acquisition process. By assuming linear CRF, image intensities in LDR images are linearly proportional to the scene radiance which forms a rank-1 matrix of LDR images. Using the rank-1 property, we have derived a rank minimization algorithm which simultaneously registers, and removes sparse outliers such as moving objects in LDR images. Since the conventional nuclear norm RPCA solution is not robust to limited number of inputs, especially for the HDR reconstruction problem where very limited number of input images are captured, we introduced the objective function based on the partial sum of singular values.

Our partial sum formulation demonstrates better HDR reconstruction than the nuclear norm formulation, and it is not biased by the magnitude of reconstructed HDR while the nuclear norm formulation favors small magnitude solutions. To this end, we have also extended our rank minimization framework to the matrix completion framework. Our matrix completion algorithm allows a user to specify masks to include particular moving objects in the reconstructed HDR image. This is achieved by considering the corresponding pixels in other LDR images as missing values.

Our proposed algorithms have been evaluated extensively on different challenging benchmark HDR datasets, and have demonstrated better performance compared with state-of-the-art HDR reconstruction algorithms. As future work, we are planning to study how to extend our method in other HDR problems, such as HDR panoramas or HDR video reconstruction.

6 ACKNOWLEDGMENT

This work was supported by the National Research Foundation of Korea(NRF) grant funded by the Korea government(MSIP) (No. 2010-0028680). In So Kweon is the corresponding author of this work.

REFERENCES

- [1] S. Mann and R. W. Picard, "On being 'undigital' with digital cameras: Extending dynamic range by combining differently exposed pictures," in *Proceedings of IS&T*, 1995, pp. 442–448.
- [2] P. E. Debevec and J. Malik, "Recovering high dynamic range radiance maps from photographs," in *Proceedings of the 24th annual conference on Computer graphics and interactive techniques*, ser. SIGGRAPH '97, 1997.
- [3] S. Hasinoff, F. Durand, and W. Freeman, "Noise-optimal capture for high dynamic range photography," in *CVPR*, 2010.
- [4] M. Granados, B. Ajdin, M. Wand, C. Theobalt, H. Seidel, and H. Lensch, "Optimal HDR reconstruction with linear digital cameras," in *CVPR*, 2010.
- [5] O. Gallo, N. Gelfand, W. Chen, M. Tico, and K. Pulli, "Artifact-free high dynamic range imaging," in *ICCP*, 2009.
- [6] S. Raman and S. Chaudhuri, "Reconstruction of high contrast images for dynamic scenes," *The Visual Computer*, vol. 27, no. 12, pp. 1099–1114, 2011.
- [7] Y. S. Heo, K. M. Lee, S. U. Lee, Y. Moon, and J. Cha, "Ghost-free high dynamic range imaging," in *ACCV*, 2010.
- [8] G. Ward, "Fast, robust image registration for compositing high dynamic range photographs from hand-held exposures," *Journal of graphics tools*, vol. 8, no. 2, pp. 17–30, 2003.
- [9] K. Jacobs, C. Loscos, and G. Ward, "Automatic high-dynamic range image generation for dynamic scenes," in *IEEE Computer Graphics and Applications*, 2008.
- [10] T.-H. Oh, J.-Y. Lee, and I. S. Kweon, "High dynamic range imaging by a rank-1 constraint," in *ICIP*, 2013.
- [11] T.-H. Oh, H. Kim, Y.-W. Tai, J. Bazin, and I. S. Kweon, "Partial sum minimization of singular values in RPCA for low-level vision," in *ICCV*, 2013.
- [12] E. Reinhard, G. Ward, S. Pattanaik, P. Debevec, W. Heidrich, and K. Myszkowski, *High Dynamic Range Imaging: Acquisition, Display, and Image-Based Lighting*, 2nd Edition. Morgan Kaufmann, 2010.
- [13] T. Mitsunaga and S. Nayar, "Radiometric self calibration," in *CVPR*, 1999.
- [14] A. Tomaszewska and R. Mantiuk, "Image registration for multi-exposure high dynamic range image acquisition," in *International Conference in Central Europe on Computer Graphics, Visualization and Computer Vision*, 2007.
- [15] S. B. Kang, M. Uyttendaele, S. Winder, and R. Szeliski, "High dynamic range video," in *ACM Transactions on Graphics (SIGGRAPH)*, vol. 22, no. 3. ACM, 2003, pp. 319–325.
- [16] B. Zitova and J. Flusser, "Image registration methods: a survey," *Image and vision computing*, vol. 21, no. 11, pp. 977–1000, 2003.
- [17] H. Zimmer, A. Bruhn, and J. Weickert, "Freehand HDR imaging of moving scenes with simultaneous resolution enhancement," in *Computer Graphics Forum*, vol. 30, no. 2. Wiley Online Library, 2011, pp. 405–414.
- [18] J. Hu, O. Gallo, K. Pulli, and X. Sun, "HDR deghosting: How to deal with saturation?" in *CVPR*, 2013.
- [19] M. D. Grossberg and S. K. Nayar, "Determining the camera response from images: What is knowable?" *IEEE Transactions on Pattern Analysis and Machine Intelligence (TPAMI)*, vol. 25, no. 11, pp. 1455–1467, 2003.

- [20] A. Agarwala, M. Dontcheva, M. Agrawala, S. Drucker, A. Colburn, B. Curless, D. Salesin, and M. Cohen, "Interactive digital photomontage," in *ACM Transactions on Graphics (TOG)*, vol. 23, no. 3. ACM, 2004, pp. 294–302.
- [21] E. Khan, A. Akyiiz, and E. Reinhard, "Ghost removal in high dynamic range images," in *ICIP*, 2006.
- [22] Y. Boykov, O. Veksler, and R. Zabih, "Fast approximate energy minimization via graph cuts," *IEEE Transactions on Pattern Analysis and Machine Intelligence (TPAMI)*, vol. 23, no. 11, pp. 1222–1239, 2001.
- [23] S. Wu, S. Xie, S. Rahardja, and Z. Li, "A robust and fast anti-ghosting algorithm for high dynamic range imaging," in *ICIP*, 2010, pp. 397–400.
- [24] W. Zhang and W.-K. Cham, "Gradient-directed multi-exposure composition," *IEEE Transactions on Image Processing (TIP)*, no. 21(4), pp. 2318–2323, 2012.
- [25] P. Sen, N. K. Kalantari, M. Yaeoubi, S. Darabi, D. B. Goldman, and E. Shechtman, "Robust Patch-Based HDR Reconstruction of Dynamic Scenes," *ACM Transactions on Graphics (TOG) (Proceedings of SIGGRAPH Asia 2012)*, vol. 31, no. 6, pp. 203:1–203:11, 2012.
- [26] N. K. Kalantari, E. Shechtman, C. Barnes, S. Darabi, D. B. Goldman, and P. Sen, "Patch-based High Dynamic Range Video," *ACM Transactions on Graphics (TOG)*, vol. 32, no. 6, 2013.
- [27] M. Granados, J. Tompkin, K. Kim, and C. Theobalt, "Automatic noise modeling for ghost-free HDR reconstruction," *ACM Transactions on Graphics (TOG)*, vol. 32, no. 6, 2013.
- [28] C. Lee, Y. Li, and V. Monga, "Ghost-free high dynamic range imaging via rank minimization," *Signal Processing Letters, IEEE*, vol. 21, no. 9, pp. 1045–1049, 2014.
- [29] S. Nayar and T. Mitsunaga, "High dynamic range imaging: Spatially varying pixel exposures," in *CVPR*, vol. 1, 2000, pp. 472–479.
- [30] J. Unger and S. Gustavson, "High-dynamic-range video for photometric measurement of illumination," *SPIE*, vol. 6501, no. 65010E, 2007.
- [31] A. Krymski, "High dynamic range imager with a rolling shutter," United States Patent No.7,397,509, 2008.
- [32] S. Nayar and V. Branzoi, "Adaptive dynamic range imaging: optical control of pixel exposures over space and time," in *ICCV*, 2003, pp. 1168–1175.
- [33] H. Wang, R. Raskar, and N. Ahuja, "High dynamic range video using split aperture camera," in *OMIVIS*, 2005.
- [34] S. Hasinoff, F. Durang, and W. Freeman, "Noise-optimal capture for high dynamic range photography," in *CVPR*, 2010.
- [35] M. Tocci, C. Kiser, N. Tocci, and P. Sen, "A versatile hdr video production system," *ACM Transactions on Graphics (TOG)*, no. 30(4), 2011.
- [36] "Magic lantern, canon dslr camera firmware, <http://www.magiclantern.fm/>," 2013.
- [37] J.-Y. Lee, Y. Matsushita, B. Shi, I. S. Kweon, and K. Ikeuchi, "Radiometric calibration by rank minimization," *IEEE Transactions on Pattern Analysis and Machine Intelligence (TPAMI)*, vol. 35, no. 1, pp. 144–156, 2013.
- [38] E. J. Candès, X. Li, Y. Ma, and J. Wright, "Robust principal component analysis?" *Journal of the ACM (JACM)*, vol. 58, no. 3, p. 11, 2011.
- [39] Y. Peng, A. Ganesh, J. Wright, W. Xu, and Y. Ma, "Rasl: Robust alignment by sparse and low-rank decomposition for linearly correlated images," *IEEE Transactions on Pattern Analysis and Machine Intelligence (TPAMI)*, pp. 2233–2246, 2012.
- [40] L. G. Brown, "A survey of image registration techniques," *ACM computing surveys (CSUR)*, vol. 24, no. 4, pp. 325–376, 1992.
- [41] M. Brown and D. G. Lowe, "Automatic panoramic image stitching using invariant features," *International Journal of Computer Vision (IJCV)*, 2007.
- [42] Z. Lin, M. Chen, and Y. Ma, "The augmented Lagrange multiplier method for exact recovery of corrupted low-rank matrices," UIUC, Tech. Rep. UILU-ENG-09-2215, 2009.
- [43] M. J. Powell, *A method for non-linear constraints in minimization problems*. UKAEA, 1967.
- [44] E. T. Hale, W. Yin, and Y. Zhang, "Fixed-point continuation for l_1 -minimization: Methodology and convergence," *SIAM Journal on Optimization*, vol. 19, no. 3, pp. 1107–1130, 2008.
- [45] D. P. Bertsekas, "Constrained optimization and lagrange multiplier methods," *Computer Science and Applied Mathematics*, Boston: Academic Press, 1982, vol. 1, 1982.
- [46] A. Srikantha and D. Sidibè, "Ghost detection and removal for high dynamic range images: Recent advances," *Signal Processing: Image Communication*, vol. 27, no. 6, pp. 650–662, 2012.
- [47] E. J. Candès and T. Tao, "The power of convex relaxation: Near-optimal matrix completion," *Information Theory, IEEE Transactions on*, 2010.
- [48] E. J. Candès and B. Recht, "Exact matrix completion via convex optimization," *Foundations of Computational mathematics*, 2009.
- [49] A. Ganesh, Z. Lin, J. Wright, L. Wu, M. Chen, and Y. Ma, "Fast algorithms for recovering a corrupted low-rank matrix," in *Computational Advances in Multi-Sensor Adaptive Processing (CAMSAP)*. IEEE, 2009.
- [50] K.-C. Toh and S. Yun, "An accelerated proximal gradient algorithm for nuclear norm regularized linear least squares problems," *Pacific Journal of Optimization*, 2010.
- [51] "Photomatrix," Commercially-available HDR processing software. <http://www.hdrsoft.com/>.
- [52] R. Achanta, A. Shaji, K. Smith, A. Lucchi, P. Fua, and S. Ssstrunk, "Slic superpixels compared to state-of-the-art superpixel methods," *IEEE Transactions on Pattern Analysis and Machine Intelligence (TPAMI)*, vol. 34, no. 11, pp. 2274–2282, 2012.
- [53] L. Wu, A. Ganesh, B. Shi, Y. Matsushita, Y. Wang, and Y. Ma, "Robust photometric stereo via low-rank matrix completion and recovery," in *ACCV*, 2011.
- [54] <http://www.hdrlabs.com/sibl/archive.html>.
- [55] T. Mertens, J. Kautz, and F. Van Reeth, "Exposure fusion: A simple and practical alternative to high dynamic range photography," in *Computer Graphics Forum*, vol. 28, no. 1. Wiley Online Library, 2009, pp. 161–171.



the IEEE.

Tae-Hyun Oh received the B.E degree (summa cum laude) in Computer Engineering from Kwang-Woon University in 2010, and the M.S degree in Electrical Engineering from KAIST in 2012. He is currently working towards the Ph.D. degree at KAIST, South Korea. He was a visiting student in the Visual Computing Group, Microsoft Research Asia. He was a recipient of Gold prize of Samsung HumanTech Thesis Award and Qualcomm Innovation Award. His research interests include robust computer vision and machine learning. He is a student member of



Joon-Young Lee received the B.S degree in Electrical and Electronic Engineering from Yonsei University, Korea in 2008, and the M.S degree in Electrical Engineering from KAIST, Korea in 2009. He is currently working toward the Ph.D. degree in Electrical Engineering at KAIST. His research interests include photometric methods in computer vision, image enhancement, and computational photography. He is a recipient of the Samsung HumanTech Paper Award and the Qualcomm Innovation Award. He is a student member of the IEEE.



Yu-Wing Tai received the Ph.D. degree from the National University of Singapore (NUS) in June 2009. He joined the Korea Advanced Institute of Science and Technology (KAIST) in Fall 2009. He regularly serves on the program committees for the major Computer Vision conferences (ICCV, CVPR and ECCV). His research interests include computer vision and image/video processing. He is a senior member of the IEEE.



In So Kweon received the BS and MS degrees in mechanical design and production engineering from Seoul National University, in 1981 and 1983, respectively, and the PhD degree in robotics from Carnegie Mellon University, 1990. He is now a professor at KAIST. He is a recipient of the best student paper runner-up award at CVPR 09'. He was the program chair for ACCV 07' and is the general chair for ACCV 12'. He is also on the editorial board of the IJCV.